Accepted Manuscript

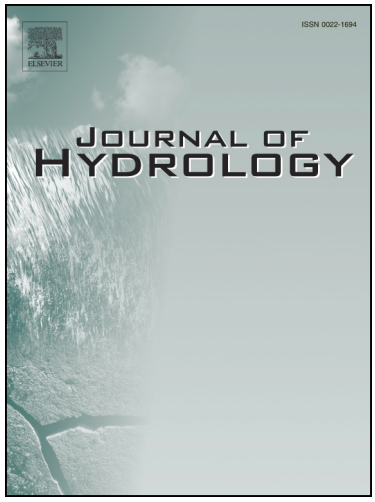

A quasi-elastic aquifer deformational behavior: Madrid aquifer case study

Pablo Ezquerro Martín, Gerardo Herrera, Miguel Marchamalo Sacristán, Roberto Tomás, Marta Béjar-Pizarro, Rubén Martínez Marín

PII: S0022-1694(14)00650-7
DOI: http://dx.doi.org/10.1016/j.jhydrol.2014.08.040
Reference: HYDROL 19837

To appear in: *Journal of Hydrology*

Received Date: 19 March 2014
Revised Date: 6 August 2014
Accepted Date: 21 August 2014

Please cite this article as: Martín, P.E., Herrera, G., Sacristán, M.M., Tomás, R., Béjar-Pizarro, M., Marín, R.M., A quasi-elastic aquifer deformational behavior: Madrid aquifer case study, *Journal of Hydrology* (2014), doi: http://dx.doi.org/10.1016/j.jhydrol.2014.08.040

A quasi-elastic aquifer deformational behavior: Madrid aquifer case study

Pablo Ezquerro Martín[a,b,e*], Gerardo Herrera[b,c,d,e], Miguel Marchamalo Sacristán[a,b,e], Roberto Tomás[c,e,f], Marta Béjar-Pizarro[b,c,e], Rubén Martínez Marín[a,e]

a Technical University of Madrid. Laboratorio de Topografía y Geomática. ETSI Caminos, Canales y Puertos C/ Profesor Aranguren s/n, 28040 Madrid, Spain, E-mail: p.ezquerro.martin@gmail.com, miguel.marchamalo@upm.es, ruben.martinez@upm.es

b Geohazards InSAR laboratory and Modeling group (InSARlab), Geoscience research department, Geological Survey of Spain (IGME), Alenza 1, E-28003 Madrid, Spain, E-mail: g.herrera@igme.es, m.bejar@igme.es

c Unidad Asociada de investigación IGME-UA de movimientos del terreno mediante interferometría radar (UNIRAD), Universidad de Alicante, P.O. Box 99, 03080 Alicante, Spain

d Earth Observation and Geohazards Expert Group (EOEG), EuroGeoSurveys, the Geological Surveys of Europe, 36-38, Rue Joseph II, 1000 Brussels, Belgium

e Grupo español de trabajo en subsidencia del terreno (SUBTER), UNESCO.

f Departamento de Ingeniería Civil, Escuela Politécnica Superior, Universidad de Alicante, P.O. Box 99, 03080 Alicante, Spain, E-mail: roberto.tomas@ua.es

* Corresponding author. E-mail address: p.ezquerro.martin@gmail.com. Telephone: +34 913366670

ABSTRACT

The purpose of this paper is to analyze the quasi-elastic deformational behavior that has been induced by groundwater withdrawal of the Tertiary detrital aquifer of Madrid (Spain). The spatial and temporal evolution of ground surface displacement was estimated by processing two datasets of radar satellite images (SAR) using Persistent Scatterer Interferometry (PSI). The first SAR dataset was acquired between April 1992 and November 2000 by ERS-1 and ERS-2 satellites, and the second one by the ENVISAT satellite between August 2002 and September 2010. The spatial distribution of PSI measurements reveals that the magnitude of the displacement increases gradually towards the center of the well field area, where approximately 80 mm of

maximum cumulated displacement is registered. The correlation analysis made between displacement and piezometric time series provides a correlation coefficient greater than 85% for all the wells. The elastic and inelastic components of measured displacements were separated, observing that the elastic component is, on average, more than 4 times the inelastic component for the studied period. Moreover, the hysteresis loops on the stress-strain plots indicate that the response is in the elastic range. These results demonstrate the quasi-elastic behavior of the aquifer. During the aquifer recovery phase ground surface uplift almost recovers from the subsidence experienced during the preceding extraction phase. Taking into account this unique aquifer system, a one dimensional elastic model was calibrated in the period 1997-2000. Subsequently, the model was used to predict the ground surface movements during the period 1992–2010. Modeled displacements were validated with PSI displacement measurements, exhibiting an error of 13% on average, related with the inelastic component of deformation occurring as a long-term trend in low permeability fine-grained units. This result further demonstrates the quasi-elastic deformational behavior of this unique aquifer system.

Keywords: DInSAR, subsidence, uplift, PSI, elastic behavior, monitoring.

1. INTRODUCTION

Subsidence caused by underground water extraction increasingly affects major cities in the world such as Mexico City (Mexico), Bologna (Italy), Houston-Galveston (USA), Tokyo (Japan), Bangkok (Thailand) and Kolkata (India) (Osmanoglu et al., 2008, Strozzi et al., 2003, Gabrysch, 1976, Yamamoto, 1995, Phien-wej et al., 2006, Chatterjee et al., 2006). The relationship between groundwater level changes and aquifer system consolidation can be explained by means of Terzaghi's effective stress principle (Terzaghi, 1925). According to the soil consolidation curve, a reduction of voids occurs in the soil (i.e. consolidation) when piezometric level declines (i.e.

effective stresses increase) inducing ground subsidence. Conversely, when piezometric levels recover (i.e. effective stress decrease), the soil undergoes an expansion that generates a surface uplift with a magnitude that depends on its deformational properties. Terzaghi's one-dimensional diffusion equation was extended by Riley (1969) and Helm (1975, 1976) to explain the aquitard drainage delay when hydraulic heads are lowered in adjacent aquifers, and the residual compaction of aquitards long after aquifer hydraulic heads are lowered. Soil deformation phenomena may produce damages on urban structures and infrastructures, causing important economic impacts on developed societies (Galloway and Burbey, 2011) and warning about the importance of monitoring those areas.

In this framework, effective and efficient subsidence monitoring is a key issue to improve prevention and mitigation within urban management strategies. Classical ground subsidence monitoring techniques are leveling topographic networks, permanent GPS measurements and extensometers (Galloway and Burbey, 2011; Tomás et al., 2014). The first two techniques measure total surface displacement, while the extensometric boreholes measure deformation of underground soil layers. However, these techniques are only able to monitor a limited amount of points due to their cost. In order to monitor large urban areas Differential Synthetic Aperture Radar Interferometry (DInSAR) and advanced DInSAR (A-DInSAR) techniques have proven to be cost effective. A-DInSAR or Persistent Scatterer Interferometry (PSI) techniques belongs to a family of algorithms based on the simultaneous processing of multiple interferograms derived from a large set of Synthetic Aperture Radar (SAR) images (Ferretti et al., 2000; Berardino et al., 2002; Mora et al., 2003; Arnaud et al., 2003; Werner et al., 2003; Hooper et al., 2004); Costantini et al., 2008). PSI techniques are able to provide dense surficial displacement measurements over large areas (Tomás et al. 2014).

The purpose of this paper is to analyze the quasi-elastic deformational behavior that has been induced by groundwater withdrawal of the Tertiary detritic aquifer of Madrid (TDAM), which is a strategic resource for the most populated city of the country. The paper is organized as follows. Section 2 introduces the TDAM. Then details about the radar satellite images, the PSI processing and the estimated displacement measurements are described. The discussion is focused firstly on the spatial and temporal analysis of measured displacements with respect to well locations and the piezometric time series. Then a one dimensional numerical elastic model is proposed and validated with PSI measurements.

2. **THE STUDY AREA**

The Madrid Metropolitan area is underlain by a large Tertiary detritic aquifer (TDAM), which has formed in a large tectonic depression (6,000 km^2) that was filled with continental deposits of Tertiary age. The boundaries of the basin (Fig. 1) are the Guadarrama Range and Somosierra ranges to the north-northwest, and the Toledo Mountains to the south. The rivers Manzanares and Henares drain this part of the basin, contributing to the Jarama River, which is tributary of Tajo River. Altitudes of the Madrid Aquifer range from 650–800 m a.s.l and the altitudes of the surrounding mountains range from 1,000–2,400 m a.s.l. According to the National Meteorological Agency (AEMET), average rainfall is between 620 mm/yr, and up to 2,000 mm/yr in the mountains. Part of it is as snow lasting several months in the north-northwest ranges. The period of July–August is dry (Hernandez-Garcia and Llamas 1995).

Palezoic schists and granites from the central mountain range bound the basin from the southwest to north, and account for the impervious basement of the aquifer. Erosional deposits of Tertiary age fill the tectonic depression, changing from northwest to southwest from detritic to evaporitic facies. These deposits result from a classic superimposed alluvial fan configuration. Low permeability sediments near the Central Range are heterogeneous in size, ranging from silts and clays to boulders. This is followed by a more permeable band made of arkosic sand lenses embedded in a clay and clay-sand matrix that constitute the main body of the TDAM (Fig. 2). These deposits gradually evolve into very low permeability evaporitic deposits towards the southeast (Martínez-Santos et al, 2010). According to Martínez-Bastida et al. (2009) and IGME (1981, 1985), TDAM is a heterogeneous and anisotropic aquifer with an average thickness of 1500 meters and variable transmissivity (1 – 852 m^2 day^{-1}) (IGME 1985). Fig. 2 shows the lithological columns of wells included along the AB cross section shown in Fig. 1. There is a clear increase of low permeability deposits towards the Pozuelo de Alarcon well field, since it is located further away from the mountain

range to the southwest, being closer to the very low permeability facies. The same transitional facies is observed in depth according to Vicente and Muñoz-Martín (2012). The contact between Intermediate Miocene sands and Lower Miocene clays or sandy clays is placed about 300 meters deep for the study area. This has been observed in most of the available boreholes, were less permeable detritic materials (clay and clay-sand matrix) are thicker with depth (Fig. 2).

(*Figure 1*)

The strongest increase in population growth for Madrid City (1900%) occurred between the 1940s and the 1970s due to rural-urban migration. From the 1970s to 1990s the population of Madrid City decreased in order to a migration from City center to metropolitan area and commuter towns. Since then metropolitan area of Madrid has experienced a steady growth and reached 3.2 million inhabitants in 2011. An additional 10% growth is expected in the next decade. Natural water supply of the city is provided by reservoirs located in the north mountain ranges (Comunidad de Madrid). The combination of drought periods and the rapid population growth (Martinez-Santos et al., 2010) has made it necessary to also exploit groundwater. Since 1970, a network of 70 wells provides water during droughts with a capacity between 60 and 80 hm^3/year. TDAM has estimated renewable resources capacity of 120-150 hm^3/year. This aquifer is additionally exploited by industries, agricultural activities and water supply of minor municipalities, accounting for 54 hm^3/year (Lopez-Camacho et al., 2006).

In this study we focus on Fuencarral and Pozuelo de Alarcón well fields located in the north-northwest of Madrid City (Fig. 1) that covers an area of 500 km^2. The former is composed by 32 wells and 26 piezometers with an average depth between 300 and 700 meters below the surface. The latter, is formed by numerous minor wells less than

200 m deep, which are usually exploited by private individuals. Therefore piezometric data is not available for these wells.

Since 1990, these well fields have undergone five cycles of extraction/recovery (Tab. 1) coinciding with drought periods. Year 2005 was extremely dry with 400 m of rain (AEMET, 2006) and provides important information during second data set. The relationship between drought and extraction periods underpins the increasing importance of aquifer management in the framework of climate change effects in major Mediterranean cities and metropolitan areas, such as Madrid.

(*Table 1*)

(*Figure 2*)

3. PSI PROCESSING AND RESULTS

3.1 SAR dataset and PSP-IFSAR processing

Persistent Scatterer Interferometry (PSI) techniques are based on the identification and exploitation on SAR images of individual radar reflectors, or persistent scatterers (PS), which are smaller than the resolution pixel cell and remain coherent over long time intervals in order to develop displacement time series (Ferretti et al., 2001). The resolution that is achieved by the identification of these PS targets effectively results in the creation of a dense data set consisting of ground ‘‘benchmarks’’ (Bell et al., 2008). The identification of stable scatterers is carried out by analyzing the time series of the radar amplitude values, and by looking for persistent, bright radar reflectors, most commonly fixed dihedral structures, such as buildings or other similar objects. The main advantages of PSI techniques are: the exploitability of most of the available SAR images since good phase coherence is obtained regardless of geometrical baseline (perpendicular separation of the satellite positions); the atmospheric phase contributions removal from the deformation phase signal through the use of an atmospheric phase screen (APS) analysis, which is determined for each radar

126 acquisition and subtracted from the total phase residuals derived from the
127 interferometry process; the generation of long deformation time series through the
128 exploitation of more than 20 radar scenes.

129 In this study two different satellite data sets obtained from the European Space Agency
130 (ESA) were processed using the PSP-IFSAR technique. The first set contains 50 ERS
131 satellite SLC SAR images in a descending track mode between April 1992 and
132 November 2000. The second set contains 31 ENVISAT satellite SLC SAR images in an
133 ascending track mode taken between August 2003 and September 2010. Selected
134 master images for image corregistration are the 7th of January 1998 for the ERS
135 dataset and the 5th of June 2007 for the ENVISAT dataset.

136 Both datasets were processed with the PSP-IFSAR technique (Costantini et al., 2008)
137 to calculate the radar line-of-sight (LOS) displacement temporal evolution of each PS
138 and to estimate the average velocity from both temporal datasets. Interferograms were
139 generated from pairs of SAR images with a perpendicular spatial baseline smaller than
140 1198 m, a temporal baseline shorter than 2089 days and a relative Doppler centroid
141 difference below 321 Hz, for both analyzed periods. The digital elevation model (DEM)
142 of the Shuttle Radar Topography Mission (SRTM) has been used to remove
143 topographic effects. The point target (PS) selection for the estimation of displacements
144 was based on a combination of several quality parameters including low amplitude
145 standard deviation and high model coherence.

146 **3.2 PSP-IFSAR results**

147 The PSP-IFSAR technique yielded 1,300,000 PS on a 100 km by 100 km area. The
148 reference points used for each period are located in a stable area 25 km northwest
149 from Madrid City. The main deformation signal detected in the study area corresponds
150 to the Fuencarral and Pozuelo Well Fields, located on the north-northwestern part of
151 TDAM. For this reason, a 40 km by 40 km subset area containing 250,000 PS centered

152 over these areas was selected to study the displacements estimates in greater detail
153 (Fig. 1).

154 During the period 1992 – 2000, the whole study area shows an average cumulated
155 displacement of -34.9 ± 22.0 mm, with values ranging from 44.1 to -144.8 mm (Fig. 4a).
156 Within this period subsidence rate accelerations coincide with aquifer extraction
157 periods, showing uplift during aquifer recovery (Table 1). The spatial analysis of the
158 retrieved displacements indicates three zones with different deformational behavior.
159 The Fuencarral extraction well field (zone 1 in Fig. 4), which is the target of this work,
160 presents a subsidence/uplift behavior that correlates well with aquifer
161 extraction/recovery periods (Fig. 6). The second zone corresponds to central-southern
162 Madrid City, which shows an overall stable behavior, with an average deformation of -
163 7.5 ± 13.2 mm (zone 2 in Figs. 4 and 6). Finally to the southwest, Pozuelo de Alarcón
164 well field (zone 3 in Figs. 4 and 6) shows a continuous subsidence behavior similar to
165 other described case studies such as Murcia City (Tomás et al., 2005; 2009; Herrera et
166 al., 2009). In this zone, during the 1992-2000 period, accelerated subsidence during
167 aquifer extraction is followed by a slower subsidence or a slight uplift during aquifer
168 recovery (Fig. 5). This elasto-plastic behavior can be explained by the greater presence
169 of clays observed in this part of the aquifer (Fig. 2) and by the higher concentration of
170 private wells exploited by local entities and individuals for water supply. Unfortunately,
171 no piezometric data are available to confirm this hypothesis.

172 The period 2003-2010 is characterized by a general uplift (2.8 ± 11.1 mm, see Table
173 1). This period includes the longest aquifer extraction episode that lasted from April
174 2005 to November 2006, and resulted in the greatest cumulative subsidence in the
175 area (17.7 ± 16.7 mm on average, see Table 1) equivalent to 12.3 mm/year subsidence
176 during 20 months (extraction 5 Fig. 6). It also includes the longest recovery period that
177 lasted from December 2006 to December 2011 and resulted in the greatest cumulative
178 uplift in the area (10.9 ± 17.2 mm on average, see Table 1) that represents 3.1

179 mm/year uplift during 60 months. Similarly to the previous time span, there are also
180 three zones that exhibit different deformational behavior. Central-southern Madrid City
181 (zone 2 in Fig. 4) remains stable (-5.5 ± 9.2 mm). Measured displacements around the
182 Fuencarral extraction well field (zone 1 in Fig. 4) showed the same fast response to
183 aquifer extraction/recovery periods (Fig. 5) exhibited in the period 1992-2000. Finally,
184 Pozuelo de Alarcón well field (zone 3 in Fig. 4) showed a slightly different deformation
185 pattern compared to the previous period. The magnitude of measured subsidence is
186 smaller and there is a slight uplift that could not be appreciated previously (Fig. 5). This
187 positive displacement (13.8 mm on average) is 4.6 times smaller than that registered in
188 Fuencarral extraction well field (63.4 mm on average). Assuming that the piezometric
189 evolution of both well fields is similar, it seems that the greater content of clays and
190 sand-clays in Pozuelo de Alarcon field (Fig. 2) is responsible for either a slower elastic
191 aquifer recovery after its exploitation, or to an elasto-plastic deformation of those clayey
192 layers. However this hypothesis cannot be evaluated in more detail because of the lack
193 of piezometric data in Pozuelo de Alarcon field and of geotechnical laboratory tests.

194 Only one permanent GPS station is available in the north edge of Fuencarral well field.
195 According to Valdes et al. (2012) GPS continuous data gathered since the beginning of
196 2009 exhibits a subsidence/uplift trend that could be related with aquifer
197 extraction/recovery phases. Even though the common temporal period is too short (5
198 months) to perform a validation both time series have been compared. The purpose of
199 this comparison is to demonstrate that within the period March to September 2010,
200 both techniques measure the same trend of the ground surface, i.e. uplift, characteristic
201 of the fifth recovery cycle of the TDAM (recovery 5 in Fig. 6). In order to do so, radar
202 ground targets (PSs) located 50 m around the GPS station have been selected and
203 averaged. Mean line of sight (LOS) displacement time series have been projected in
204 the vertical direction so they are comparable with GPS vertical measurements. A good
205 agreement can be observed between the PSI and GPS measurements (Fig. 3), since

206 they both measure the same uplift trend, identifying similar acceleration and
207 deceleration events.

208 (*Figure 3*)

209 (*Figure 4*)

210 (*Figure 5*)

211

212 **4. Analysis of aquifer system exploitation cycles**

213 **4.1. Regional analysis**

214 The influence area of the aquifer system exploitation has been assessed by the
215 relationship between the differential displacements measured for every extraction-
216 recovery phase with respect to the distance to the wells (Fig. 6a). For this purpose in
217 every extraction/recovery cycle, we have computed the average differential
218 displacement measured in those PSs included within different buffer areas defined by a
219 distance from the wells varying from 500 to 10,000 m. As it is shown in Fig. 6b, ground
220 displacement was rather homogeneous and intense from 500 to 4,000 m, reaching a
221 nearly stable behavior from 7,000 m to 10,000 m. Therefore, the greatest influence
222 area of the aquifer exploitation is limited to the 4,000 m radius circle around the wells
223 and to a lower extent, within 7,000 m.

224 (*Figure 6*)

225 The overall balance of the differential displacement measured for every
226 extraction/recovery cycle within the 4,000 m radius influence area reveals a regional
227 subsidence of 31.8 mm (Table 2) and 22.9 mm excluding cycles 3 and 4, which were
228 not fully covered by SAR images. This balance was reduced to a 22.7 and 16.2 mm
229 subsidence, respectively, measured within 500 m distance from the wells (Table 2).
230 These results evidenced that aquifer exploitation in the period 1992 – 2010, produced a

231 regional 20-30 mm subsidence that was smaller (10-20 mm) nearby the wells, where a
232 greater uplift was measured during the recovery phases.

233 (*Table 2*)

234 The relationship between differential ground surface displacement and the duration of
235 the extraction-recovery phases for every cycle has been also analyzed. For this
236 purpose the uplift - subsidence ratio (SR) and the cycle temporal ratio (TR) were
237 calculated (Table 2). The SR represents the ratio between ground surface uplift (δ_{uplift})
238 measured during the recovery phase with respect to the subsidence (δ_{subs}) measured in
239 the extraction phase (i.e. $\delta_{uplift}/\delta_{subs}$) expressed in percentage. The TR corresponds to
240 the relationship between the duration of the recovery (t_{recov}) over the duration of the
241 extraction ($t_{extract}$) also expressed in percentage (i.e. $t_{recov}/t_{extract}$). According to current
242 management practices, TR should be between 2 and 4 for a good aquifer recovery.

243 For the first cycle, ground surface subsidence associated with the extraction phase
244 decelerated during the recovery phase, when no net uplift was measured (SR=0%,
245 TR=0.9). In the cycle 2 recovery phase, there was a clear uplift that compensates both
246 the subsidence produced during the extraction phase of cycle 2 and part of the first one
247 (SR=126% and TR=3.7). The third and fourth cycles cannot be analyzed because the
248 satellite data for these periods were incomplete. Cycle number 5 includes the longest
249 extraction that produced the greatest subsidence in whole period 1992-2010, followed
250 by a long recovery phase responsible for an uplift that compensated 75% of the
251 previous subsidence (SR=75%, TR=3). This analysis suggests that for this aquifer
252 system, the greater the cycle temporal ratio the greater the uplift-subsidence ratio.

253 **4.2. Temporal analysis and modeling**

254 Displacement time series obtained from the analysis of ERS SAR images (1992-2000)
255 and ENVISAT SAR images (2003-2010) were compared with water level data available
256 for the period 1997-2010 for 17 wells (Fig. 9). For this purpose the average

displacement time series of all the PS located closer than 500 m around each well have been calculated. A high correlation coefficient (r) is observed between displacement time series and water level variation ranging from 0.64 to 0.92, with an average value of 0.85 ± 0.07. A quasi-elastic deformational behavior of the aquifer system can be assumed taking into account the great linear correlation obtained between piezometric level changes and aquifer system displacements. As a first approximation, the inelastic component of deformation occurring as a long-term trend in low permeability fine-grained units is removed from the stress-strain data (Fig. 7) following Sneed and Galloway (2000). Moreover the elastic/inelastic deformation ratio ($R_{ed/id}$) was calculated (Tab. 3). The inelastic component was calculated as the slope of the line fitted by a minimum square regression multiplied by the monitoring time span. The elastic component represents the difference between the maximum and minimum deformation measured during the monitoring period (i.e. the maximum amplitude of the displacements measured during the different extraction-recovery phases for the monitored period). Values higher than 1 indicates a dominant elastic behavior and positive values a predominantly inelastic behavior. In the case of the TDAM, this ratio range from 1,66 to 10,36. Thus the elastic component is on average 4,34 times the inelastic component of TDAM deformation.

For this reason we assume that aquifer system pore pressure (or hydraulic head) quickly equilibrates with piezometric level changes of the most permeable layers, proposing a one-dimensional elastic model to simulate ground subsidence due to water level changes. Note that this assumption implies no consolidation when the piezometric level is stable. Also the delay between hydraulic head changes and aquifer system deformation would not be significant, as can be seen in Figs. 8 and 9.

(Figure 7)

Consequently, the vertical displacements (δ) only depend on the magnitude of the hydraulic head change (Δh) and the deformational properties of the aquifer system. Hence, modifying the equation proposed by Hoffman (2003, eq. 2.15):

$$\delta = \Delta h \times S_{sk} \times D = \Delta h \times S_k \quad (1)$$

where S_{sk} is the the skeletal specific storage, D is the aquifer system thickness, and S_k is the skeletal storage coefficient (dimensionless) of the aquifer system. S_{sk} and S_k are related with the widely used storage coefficient, S, by means of:

$$S = S_s \times D = (S_{sk} + S_{sw}) \times D \quad (2)$$

where S_{sw} is the water specific storage, and S_s is the specific storage defined as the volume of water expelled per unit area from a layer of thickness D due to a unit decline in the hydraulic head (Todd, 1980). Note that in an aquifer system, water is derived from two processes (e.g. Sneed and Galloway, 2000): a) void changes, which causes the compaction or expansion of the aquifer system caused by the effective stress changes, and; b) from the expansion or compression of the water owing to a change in pore pressure. The first process, which for unconsolidated aquifer systems is the dominant process, is controlled by the skeletal specific storage, and strongly depends of the grain-size of the aquifer system. For aquitards S_{sk} from equation (1) represents the deformability of the aquitards and varies with the stress state (Sneed and Galloway, 2000). When the stress induced by the hydraulic head variation exceeds the maximum preexisting stress, i.e. preconsolidation stress, deformations are very high and mainly irrecoverable due to soil rearrangement and compaction. However, if induced stress does not exceed the preconsolidation stress the deformations are much smaller and mostly elastic. This different soil behavior can be introduced to eq. (1) by assigning two different skeletal specific storages, elastic (S_{ske}) and anelastic (S_{skv}), according to to the state of stress with respect to the preconsolidation stress. However, typically for coarse-grained deposits within aquifers inelastic deformation is negligible and S_{ske} is

used regardless of the preconsolidation stress (Sneed and Galloway, 2000).In this case study, as previously mentioned, the aquifer system exhibits a clear elastic behavior, the piezometric seasonal changes present similar amplitudes, and the soil is mainly composed of coarse material (sands). Consequently, eq. (1) is rewritten as:

$$\delta = \Delta h \times S_{ske} \times D = \Delta h \times S_{ke} \quad (3)$$

Where S_{ke} can be computed by means of the graphical methodology proposed by Riley (1969), which consists of the determination of the slope of the stress–strain curve branch (the elastic branch in this case). Note that this methodology for computing storage coefficients has been widely used by other authors using InSAR derived and borehole extensometers derived displacements (Hanson, 1989; Sneed and Galloway, 2000; Hoffman, 2003; Hoffmann et al., 2003; Burbey, 2003; Tomás et al., 2006; Galloway and Hoffmann, 2007; Zhang et al., 2007a,b; Tomás et al., 2010).

In this work, the elastic storage coefficients S_{ke} of aquifer has been computed for the period 1997-2000 using piezometric series for the 17 available wells where DInSAR retrieved deformations are also known (Fig. 8). These data allowed plotting the stress-strain curves that represent the relationship between piezometric level changes and aquifer system deformations, from which elastic storage coefficients were determined following the expression:

$$S_{ke} = \frac{\Delta D}{\Delta h} \quad (4)$$

Where ΔD is the displacement caused by a Δh piezometric level decrease. S_{ke} was calculated during the third extraction of each well as shown in Fig. 8.

Additionally, the aquifer storage coefficient (S), commonly used in the groundwater flow equation, was calculated as:

$$S = S_w + S_{ke} = S_{sw} \times b + S_{ke} \quad (5)$$

Where S_{sw} is:

$$S_{sw} = (n \times \gamma) / E_w \quad (6)$$

where n is the porosity of the aquifer (varying from 1 to 20% according to Rodriguez, 2000), γ is the unit weight of water (9.81 x 10^3 N/m^3), Ew is the bulk modulus of elasticity of water (2.15 x 10^9 Pa) and b the thickness of the aquifer layers. S was computed only in those wells where lithological data were available (Tab. 3).

(*Figure 8*)

The hysteresis loops on the stress-strain plot (Figure 8) indicate that the response is in the elastic range. The loops correspond to the aquifer extraction and recovery periods. As it can be seen, data dispersion is low, indicating that there is a good temporal correlation and a small irrecoverable compaction (Zhang et al., 2013). This fact indicates that the aquifer system exhibits a quasi-elastic behavior. The computation of S_{ke} has been performed considering the extraction phase of the first cycle (Fig. 8). The computed elastic storage coefficients (S_{ke}) for the available wells of the TDAM vary from 1.12×10^{-4} to 4.68×10^{-4}, with an average value of $2.99\times10^{-4} \pm 9.30\times10^{-5}$ (Tab. 3). Taking into account the sandy composition of TDAM, the S_{ke} has been considered to predict subsidence from the rest of the piezometric level time series (1997-2010). In the Following, DInSAR data are used to validate the robustness of the model.

(*Table 3*)

Fig. 9 shows modeled and DInSAR based displacement time series for six wells, whereas the statistics of the comparison between the model and DInSAR values is summarized in Table 4. The average absolute difference between DInSAR and modeling time series is of 8.2 ± 2.8 mm, being defined as a quality indicator of the fit

between both time series. This error has been compared with the maximum measured DINSAR displacement for every well (Table 4). Consequently, an average relative error of 13 ± 3% has been obtained for all the wells considering the period from 1997 to 2010. Excluding the calibration period (1997-2000) this relative error increases slightly to 16 ± 4%. However, this error is clearly observed in the 2005-2007 extraction cycle, where the model underestimates ground settlements measured with DInSAR. This mismatch between both time series can be related to the duration of this extraction cycle (20 months), which is 1.5 times the extraction cycle from the period 1999-2000 (13 months). A longer duration of the extraction cycle permits the aquitards composed by less permeable materials (clays and clay-sands) gradually to reduce water pore pressure, increasing effective stress and producing a greater consolidation of these materials than in shorter extraction cycles. However, even though the extraction cycle duration was 53% longer, there is only a 13 ± 3% error in the model–DInSAR time series comparison. This fact is specially noted in FA-1, FC-2 and FE-1 wells, where the clay & clay-sand percentage is 25% greater than in the rest. For instance in the wells depicted in Fig. 9 this content varies from 25% in the North East of the study area (CB-6) to the 68% in the South West (PM-7).

(*Table 4*)

(*Figure 9*)

5. Discussion and Conclusions

Most of the available literature case studies describe plastic or elasto-plastic aquifer deformation. These aquifers are usually overexploited and exhibit a continuous piezometric decline together with seasonal variations that are responsible for continuous plastic deformation and cyclic elastic deformations. Galloway and Hoffmann (2007) reviewed the deformational behavior of several aquifer systems in United States. In Antelope Valley (California) 10 m seasonal ground water level changes

triggered a ±5 mm elastic deformation and a plastic deformation that reached 60 mm after 4 years. In other works, intermittent extractions triggered a deceleration of ground surface response. Liu et al. (2004b) described cumulated subsidence of 1.8 m related to a 30 m decrease of groundwater level during 20 years in a multilayer aquifer system in Taiwan. During this time span subsidence deceleration could be explained by a smaller groundwater level decline. Liu et al. (2004a) observed that although the piezometric level of the Choshui River alluvial fan aquifer system increased, ground uplift was not observed. Zhang et al. (2013) described subsidence phenomenon in the multilayer confined aquifer of Beijing city plain. In this case Long term deformation (80 cm in the past 40 years) was related to a historical groundwater level drawdown of 20 m. This elasto-plastic deformation occurred mainly below 60 m deep, whereas in the surficial aquitard and aquifer layers a ±2 mm elastic deformation was triggered instantaneously by 10 meters of groundwater level variation.

In our particular case study, TDAM exhibits a quasi-elastic aquifer deformational behavior induced by groundwater withdrawal affecting the Tertiary detritic aquifer of Madrid (Spain). The spatial and temporal evolution of ground surface displacement was estimated processing two datasets of radar satellite images (SAR) using Persistent Scatterer Interferometry (PSI) from April 1992 to October 2000 and from August 2003 to September 2010. Note that although the PSI techniques assumed a linear model of deformation during the processing, many examples exist of detection of non-linear component inside the PS time series, confirming the power of PSI to monitor ground deformation (Ferretti et al. 2000, Cigna et al. 2011, Tofani et al. 2013). Cyclic and quasi-elastic ± 80 mm deformation triggered by 120 to 200 m cyclic water level changes was higher near well fields and decreases with the distance. Differently from previous case studies, groundwater drawdown was caused by long extraction cycles (10-20 months) produced during drought periods. High correlation coefficient between piezometric level changes and surficial displacement demonstrate a high permeability

of the aquifer that favors fast pore water pressure dissipation. Furthermore, a quasi-elastic behavior was observed in Fuencarral well field area where the sandy component of the aquifer is dominant. In this area, when groundwater level drops the aquifer is continuously deformed, being recovered when the groundwater level rebounds. In Pozuelo de Alarcon well field, an elasto-plastic deformation was appreciated probably due to the higher clay percentage of the different layers from the aquifer system observed in this part of the basin.

Different aquifer subsidence models have been implemented by Gambolati (1975), Gambolati et al. (2001), Xue et al. (2008), Wu et al. (2009), Herrera et al. (2009), Tomás et al. (2009), Luo and Zeng (2011) and Raspini et al. (2014) among others. The selection of the most convenient model for predicting subsidence depends on several complex factors and on the local geological conditions, which can vary from place to place (Hu et al., 2002). However, under certain conditions, simpler models have demonstrated to be useful for this task. In this case study, due to the lack of soil parameters, we implemented a one-dimensional elastic model following the work published by Tomas et al. (2009). In our model cyclic hydraulic changes were instantaneous across the whole aquifer system due to its dominant sandy nature, being deformations (subsidence and uplift) directly related to these changes. Therefore on the basis of the elastic storage coefficient (S_{ke}) of the aquifer system we assumed a linear elastic behavior. The comparison of computed displacements with respect to DInSAR displacement measurements revealed a good agreement, being 8.2±2.8 mm and 13%, respectively, the average and the percentage error of the proposed model.

These results evidence the quasi-elastic aquifer deformational behavior induced by groundwater withdrawal of the Tertiary detritic aquifer of Madrid (Spain). Groundwater management exploitation practice seems adequate since the piezometric level recovers well after every extraction period. Moreover, detected displacements reveal a moderate subsidence phenomenon affecting a wide area of 500 km^2 on the north-west

435 of Madrid metropolitan area, where no major damages have been acknowledge on
436 urban structures and infrastructures. In the near future, the integration of both the PSI
437 monitoring techniques and aquifer numerical models will permit to predict subsidence
438 in further drought periods, which are expected to increase in the context of climate
439 change evolution and population growth. They could be also a tool to evaluate the
440 effectiveness of mitigation measurements eventually adopted in subsidence-affected
441 areas.

442

443 **Acknowledgements**

444 This work was developed during Pablo Ezquerro research stay within the Geohazards
445 InSAR laboratory and Modeling group of the Instituto Geológico y Minero de España in
446 the framework of DORIS project (Ground Deformation Risk Scenarios: an Advanced
447 Assessment Service) funded by the EC-GMES-FP7 initiative (Grant Agreement
448 n°242212). This work has been also supported by the Spanish Ministry of Science and
449 Research (MICINN) under project TEC2011-28201-C02-02 and EU FEDER. Authors
450 want to acknowledge reviewers J.A. Huisman, Devin L. Galloway and Federico
451 Raspini, and editor Peter K. Kitanidis for their valuable contributions to improve the
452 quality of this paper.

453

454 **REFERENCES**

455 Amelung, F., Galloway, D., Bell, J., Zebker, H., Laczniak, R., 1999. Sensing the ups
456 and downs of Las Vegas: InSAR reveals structural control of land subsidence and
457 aquifer-system deformation. Geology. 6, p. 483–486.

458 Arnaud, A., Adam, N.,Hanssen, R., Inglada, J.,Duro, J., Closa, J., Eineder, M., 2003.
459 ASAR ERS interferometric phase continuity. Proc. IEEE International Geoscience and

460 Remote Sensing Symposium (IGARSS-03), 21–25 July, Toulouse, France, vol. 2, pp.
461 1133–1135.

462 Bawden, G., Thatcher, W., Stein, R., Hudnut, K., Peltzer, G., 2001. Tectonic
463 contractions across Los Angeles after removal of groundwater pumping effects. Nature.
464 412, 812–815.

465 Bell, J.W., Amelung, F., Ferretti, A., Bianchi, M., Novali, F., 2008. Permanent scatterer
466 InSAR reveals seasonal and long-term aquifer-system response to groundwater
467 pumping and artificial recharge. Water Resour. Res. 44, 1–18.

468 Berardino, P., Fornaro, G., Lanari, R., Sansosti, E., 2002. A new algorithm for surface
469 deformation monitoring based on small baseline differential SAR interferograms. IEEE
470 Trans. Geosci. Remote Sens. 40, 2375–2383.

471 Lopez-Camacho, B., Iglesias, J.A., Sanchez,E., 2006. El campo de pozos del
472 Guadarrama: Un proyecto innovador del Canal de Isabel II para el aprovechamiento de
473 aguas subterráneas. III Congreso de ingeniería civil, territorio y medio ambiente.
474 Zaragoza, 26-28 October 2006.

475 Burbey, T.J., 2003. Use of time-subsidence data during pumping to characterize
476 specific storage and hydraulic conductivity of semiconfining units. J. Hydrol. 281, 3–22.

477 Casu, F., Manzo, M., Lanari, R.A., 2006. Quantitative assessment of the SBAS
478 algorithm performance for surface deformation retrieval from DInSAR data. J. Remote
479 Sens. Environ. 102, 195–210.

480 Chatterjeea, R.S., Fruneaub, B., Rudantb, J.P., Royc, P.S., Frisonb, P.L., Lakheraa,
481 R.C., Dadhwala, V.K., Saha, R., 2006. Subsidence of Kolkata (Calcutta) City, India
482 during the 1990s as observed from space by Differential Synthetic Aperture Radar
483 Interferometry (D-InSAR) technique. Remote Sensing of Environment 102, 176 – 185

484 Cigna, F., Del Ventisette, C., Liguori, V., Casagli, N., 2011. Advanced radar-
485 interpretation of InSAR time series for mapping and characterization of geological
486 processes. Natural Hazards Earth System Science 11, 865-881.

487 Colesanti, C., Ferretti, A., Novali, F., Prati, C., Rocca, F., 2003. SAR Monitoring of
488 progressive and seasonal ground deformation using the permanent scatterers
489 technique. IEEE Trans. Geosci. Remote 41, 1685–1701.

490 Costantini, M., Falco, S., Malvarosa, F., Minati, F., 2008. A new method for
491 identification and analysis of persistent scatterers in series of SAR images. Int. Geosci.
492 Remote Sensing Symp. (IGARSS). 449-452.

493 Ferretti, A., Prati, C., Rocca, F., 2000. Nonlinear subsidence rate estimation using
494 permanent scatterers in differential SAR interferometry. IEEE Trans. Geosci. Remote
495 Sens. 38, 2202–2212.

496 Ferretti, A., C. Prati, and C. Rocca, 2001. Permanent scatterers in SAR interferometry,
497 IEEE Trans. Geosci. Remote Sens., 39(1), 8 –20.

498 Ferretti, A., Novali, F., Bürgmann, R., Hilley, G., Prati, C., 2004. InSAR permanent
499 scatterer analysis reveals ups and downs in San Francisco Bay Area. EOS 85, 317–
500 324.

501 Gabrysch, R.K., 1976. Land-surface subsidence in the Houston-Galveston Region,
502 Texas. Publication n°121 of the International Association of Hydrological Sciences
503 Proceedings of the Anaheim Symposium.

504 Galloway, D.L., Hoffmann, J., 2007. The application of satellite differential SAR
505 interferometry-derived ground displacements in hydrogeology. Hydrogeol. J. 15, 133–
506 154.

507 Galloway, D., Burbey, T., 2011. Review: Regional land subsidence accompanying
508 groundwater extraction. Hydrogeology Journal 19, 1459-1486.

509 Galloway, D., Jones, D.R., Ingebritsen, S.E. (1999). Land Subsidence in the United
510 States. U.S. Geological Survey Circular 1182. Available in:
511 http://pubs.usgs.gov/circ/circ1182/#pdf

512 Gambolati, G., 1975. Numerical models in land subsidence control. Comput. Methods
513 Appl. Mech. Eng. 5, 227–237.

514 Gambolati, G., Ferronato, M., Teatini, P., Deidda, R., Lecca, G., 2001. Finite element
515 analysis of land subsidence above depleted reservoirs with pore pressure gradient and
516 total stress formulations. Int. J. Numer. Anal. Methods Geomech. 25, 307–327.

517 González, P.J., Fernández, J., 2011. Drought transient aquifer compactation imaged
518 using multitemporal satellite radar. interferometry. Geology. 39, 551–554

519 Hanson, R.T., 1989. Aquifer-system compaction, Tucson Basin and Avra Valley,
520 Arizona: U.S. Geological Survey Water-Resources Investigations Report 88-4172, 69
521 p., http://pubs.er.usgs.gov/publication/wri884172

522 Helm, D.C. (1975) One-dimensional simulation of aquifer system compaction near
523 Pixley, Calif. 1: constant parameters. Water Resour Res 11(3):465–478.

524 Helm, D.C. (1976) One-dimensional simulation of aquifer system compaction near
525 Pixley, Calif. 2: stress-dependent parameters. Water Resour Res 1(3):375–391

526 Herrera, G., Fernandez-Merodo, J., Tomás, R., Cooksley, G., Mulas, J., 2009.
527 Advanced interpretation of subsidence in Murcia (SE Spain) using A-DInSAR data-
528 modelling and validation. Nat. Hazards Earth Syst. Sci. 9, 647–661.

529 Hoffmann, J., Zebker, H. A., Galloway, D. L., Amelung, F., 2001. Seasonal subsidence
530 and rebound in Las Vegas Valley, Nevada, observed by synthetic aperture radar
531 interferometry, Water Resour. Res. 37(6),1551– 1566.

532 Hoffman, J., 2003. The application of satellite radar interferometry to the study of land
533 subsidence over developed aquifer systems. PhD Thesis, University of Stanford, 211
534 pp.

535 Hoffmann, J., Galloway, D.L., Zebker, H.A., 2003. Inverse modeling of interbed storage
536 parameters using land subsidence observations, Antelope Valley, California. Water
537 Resour. Res. 39, 5–10.

538 Hooper, A., Zebker, H., Segall, P., Kampes, B., 2004. A new method for measuring
539 deformation on volcanoes and other natural terrains using InSAR Persistent Scatterers.
540 Geophys. Res. Lett. 31.

541 Hu, R.L., Wang, S.J., Lee, C.F., Li, M.L., 2002. Characteristics and trends of land
542 subsidence in Tanggu, Tianjin, China. Bull. Eng. Geol. Environ. 61, 213–225.

543 Instituto Geológico y Minero de España (IGME), 1981. Plan Nacional de Investigación
544 de Aguas Subterráneas (PNIAS): Proyecto de investigación hidrogeológica de la
545 cuenca del Tajo. Informes técnicos 1–5 [National Plan for Groundwater Research
546 (PNIAS). Research Project on the hydrogeology of the Tajo basin. Technical reports 1–
547 5]. IGME, Madrid

548 Instituto Geológico y Minero de España (IGME) (1985) Calidad y contaminación de las
549 aguas subterráneas en España [Groundwater quality and groundwater contamination
550 in Spain]. Informe de síntesis, Tomo II, Anejos, IGME, Madrid, 385 pp. Available on the
551 Internet. http://aguas.igme.es/igme/publica/libro43/lib43.htm. March 2008

552 Liu, C.-H., Pan, Y.-W., Liao, J.-J., Huang, C.-T., Ouyang, S., 2004a. Characterization of
553 land subsidence in the Choshui River alluvial fan, Taiwan. Enviromental Geology. 45,
554 1154–1166.

555 Liu, C.-H., Pan, Y.-W., Liao, J.-J., Hung, W.-C., 2004b. Estimating coefficients of
556 volume compressibility from compression of strata and piezometric changes in a
557 multiaquifer system in west Taiwan. Eng. Geol. 75, 33–47.

558 Liu, Y., Huang, H-J., 2013. Characterization and mechanism of regional land
559 subsidence in the Yellow River Delta, China. Natural Hazards. 68, 687–709.

560 Luo, Z.- J., Zeng, F., 2011. Finite element numerical simulation of land subsidence and
561 groundwater exploitation based on visco-elastic-plastic biot's consolidation theory.
562 Journal of Hydrodynamics, Ser. B 23, 615-624.

563 Martínez-Bastida, J.J., Arauzo, M., Valladolid, M., 2009. Intrinsic and specific
564 vulnerability of groundwater in central Spain: the risk of nitrate pollution. Hydrogeology
565 Journal, 18 681 – 698.

566 Martínez-Santos, P., Pedretti, D., Martínez-Alfaro, P.E., Conde, M., Casado, M., 2010.
567 Modelling the Effects of Groundwater-Based Urban Supply in Low-Permeability
568 Aquifers: Application to the Madrid Aquifer, Spain. Water Resour Manage, 24 4613 –
569 4638.

570 Mora, O., Mallorquí, J.J., Broquetas, A., 2003. Linear and nonlinear terrain deformation
571 maps from a reduced set of interferometric SAR images. IEEE Trans. Geosci. Remote
572 41, 2243–2253.

573 Navarro, A., Fernández, A., Doblas, J.G. Las aguas subterráneas en España. IGME.
574 1993.

575 Osmanoglu, B., Dixon, T. H., Cabral-Cano, E., Wdowinski, S., 2008. Mexico City
576 Subsidence. American Geophysical Union, Fall Meeting 2008.

577 Phien-wej, N., Giao, P.H., Nutalaya, P., 2006. Land subsidence in Bangkok, Thailand.
578 Engineering Geology 82, 187 – 201.

579 Poland, J.F., and Davis, G.H., 1969. Land subsidence due to withdrawal of fluids, in
580 Varnes, D.J., and Kiersch, G., eds. Reviews in engineering geology, v.2. Geol. Soc.
581 America, p. 187-269.

582 Poland, J.F., 1984. Guidebook to studies of land subsidence due to ground-water
583 withdrawal. Technical report, UNESCO.

584 Raspini, F., Loupasakis, C., Rozos, D., Adam, N., Moretti, S., 2014. Ground
585 subsidence phenomena in the Delta municipality region (Northern Greece):
586 Geotechnical modeling and validation with Persistent Scatterer Interferometry.
587 International Journal of Applied Earth Observation and Geoinformation, 28 78 – 89.

588 Riley, F.S., 1969. Analysis of borehole extensometer data from central California. In:
589 Tison LJ (ed) Land subsidence. Proceedings of the Tokyo Symposium, Sept 1969,
590 IAHS Pub. 88:423–431. http://iahs.info/redbooks/a088/088047.pdf.

591 Rodríguez, J.M., 2000. Propiedades geotécnicas de los suelos de Madrid. Revista de
592 Obras Públicas. 3405, pp 59-84.

593 Sneed, M., Galloway, D.L., 2000. Aquifer-system compaction and land subsidence:
594 measurements, analyses, and simulations: the Holly site, Edwards Air Force Base,
595 Antelope Valley, California. US Geol Surv Water-Resour Invest Rep 00–4015.
596 http://pubs.usgs.gov/wri/2000/wri004015/. 65 pp.

597 Strozzi, T., Wegmuller, U., Werner, C.L., Wiesmann, A., Spreckels, V., 2003. JERS
598 SAR interferometry for land subsidence monitoring. Geoscience and Remote Sensing
599 41 7Terzaghi K (1925) Settlement and consolidation of clay. McGraw-Hill, New York,
600 pp 874–878.

601 Todd, D.K., 1980. Groundwater Hydrology. John Wiley & Sons, New York, 2 edition.

602 Tofani, V., Raspini, F., Catani, F., Casagli, N., 2013. Persistent Scatterer Interferometry
603 (PSI) Technique for Landslide Characterization and Monitoring. Remote Sensing 5,
604 1045-1065.

605 Tomás, R., Márquez, Y., Lopez-Sanchez, J.M., Delgado, J., Blanco, P., Mallorqui, J.J.,
606 Martinez, M., Herrera, G., Mulas, J., 2005. Mapping ground subsidence induced by
607 aquifer overexploitation using advanced Differential SAR Interferometry: Vega Media of
608 the Segura River (SE Spain) case study. Remote Sensing of the Environment 98, 269–
609 283.

610 Tomás, R., Herrera, G., Delgado, J., Lopez-Sanchez, J.M., Mallorquí, J.J., Mulas, J.,
611 2009. A ground subsidence study based on DInSAR data: Calibration of soil
612 parameters and subsidence prediction in Murcia City (Spain). Engineering Geology
613 111, 19-30.

614 Tomás, R., Romero, R., Mulas, J., Marturià, J.J., Mallorquí, J.J., Lopez-Sanchez, J.M.,
615 Herrera, G., Gutiérrez, F., González, P.J., Fernández, J., Duque, S., Concha-Dimas,
616 A., Cocksley, G., Castañeda, C., Carrasco, D., Blanco, P., 2014. Radar interferometry
617 techniques for the study of ground subsidence phenomena: a review of practical issues
618 through cases in Spain. Environmental Earth Sciences 71, 163-181.

619 Tomás, R., Lopez-Sanchez, J.M., Delgado, J., Mallorquí, J.J., 2006. Hydrological
620 parameters of the Vega Media of the Segura River Aquifer (SE Spain) obtained by
621 means of advanced DInSAR. IEEE International Conference on Geoscience and
622 Remote Sensing Symposium, 2006 (IGARSS 2006), July 31–Aug. 4, pp. 1553–1556.

623 Valdés, M., Cano, M.A., Pascual, M., García-Cañada, L., 2012. Análisis de estaciones
624 permanentes GNSS de la península ibérica, proyecto IBERRED. 7ª Asamblea
625 Hispano-Portuguesa de geodesia y geofísica.

626 Vicente, G., Muñoz-Martín, A., 2013. The Madrid Basin and the Central System: A
627 tectonostratigraphic analysis from 2D seismic lines. Tectonophysics. 602, 259–285

628 Werner, C., Wegmüller, U., Strozzi, T., Wiesmann, A., 2003. Interferometric point target
629 analysis for deformation mapping. Proc. IEEE International Geoscience and Remote
630 Sensing Symposium (IGARSS-03), 21–25 July, Toulouse. France 7, 4362–4364.

631 Wu, J., Shi, X., Ye, S., Xue, Y., Zhang, Y., Yu, J., 2009. Numerical simulation of land
632 subsidence induced by groundwater overexploitation in Su-Xi-Chang area. China.
633 Environ. Geol. 57, 1409–1421. Xu, Y., Shen, S., Cai, Z., Zhou, G., 2008. The state of
634 land subsidence and prediction approaches due to ground water withdrawal in China.
635 Nat. Hazards 45, 123–135.

636 Xu, Y., Shen, S., Cai, Z., Zhou, G., 2008. The state of land subsidence and prediction
637 approaches due to ground water withdrawal in China. Nat. Hazards 45, 123–135.

638 Yamamoto, S., 1995. Recent trend of land subsidence in Japan. Land subsidence 234.

639 Zhang, Y., Xue, Y.-Q., Wu, J.-C., Ye, S.-J., Li, Q.-F., 2007a. Stress–strain
640 measurements of deforming aquifer system that underlie Shanghai, China. Environ.
641 Eng. Geosci. XIII, 217–228.

642 Zhang, Y., Xue, Y.-Q., Wu, J.-C., Ye, S.-J., Wei, Z.-W., Li, Q.-F., Yu, J., 2007b.
643 Characteristics of aquifer system deformation in the Southern Yangtse Delta. China.
644 Eng. Geol. 90, 160–173.

645 Zhang, Y., Gong, H., Gu, Z., Wang, R., Li, X., Zhao, W., 2013. Characterization of land
646 subsidence induced by groundwater withdrawls in the plain of Beijing city, China.
647 Hidrogeology Journal.

648 Zerbini, S., Richter, B., Rocca, F., Van Dam, T., Matonti, F., 2007. A combination of
649 space and terrestrial geodetic techniques to monitor land subsidence: case study, the
650 Southeastern Po Plain, Italy. J. Geophys. Res. 112, B05401.

651 **Web**

652 Agencia Estatal de Meteorología (AEMET). Resumen anual climatológico de 2005.
653 http://www.aemet.es/es/serviciosclimaticos/vigilancia_clima/resumenes. Last access:
654 18/03/2014

655 Agencia Estatal de Meteorología (AEMET) Web.
656 http://www.aemet.es/es/serviciosclimaticos/datosclimatologicos. Last access:
657 18/03/2014

658 Madrid City Hall Web.
659 http://www.madrid.es/portales/munimadrid/es/Inicio/Ayuntamiento/Estadistica/Demogra
660 fia-y-
661 Poblacion?vgnextfmt=default&vgnextchannel=dfd9ef637004a010VgnVCM100000d90c
662 a8c0RCRD. Last access: 18/03/2014

663 Comunidad de Madrid: Infraestructuras de Abastecimiento de la Comunidad de Madrid
664 (Water supply infrastructures of the Community of Madrid)

665 http://www.madrid.org/cs/Satellite?c=CM_InfPractica_FA&cid=1114178464601&idTem
666 a=1142598825576&language=es&pagename=ComunidadMadrid%2FEstructura&pid=
667 1273078188154&pv=1114178871983

668

Figure 1. a) Geological map and b) cross sections of the study area.

Figure 2. Illustration of the lithological logs of the wells from the study area. Upper line corresponds to ground surface and medium and lower lines indicate the position of the piezometric level maximum and minimum depths, respectively, across the cross section. Low permeability lithologies (fine clayed sands and clays) are represented in black while high permeability lithologies (medium-coarse sands) are represented in white. Wells location is shown in Figure 1. Grey marks left side of the logs shows the position of the productive areas of each well.

Figure 3. DInSAR – GPS comparison around Tres Cantos GPS Station (3CAN). Note that both series have different origin.

Figura 4. a) Cumulated displacements from April 19th 1992 b) Cumulated deformation from August 5th 2003. Blue labels in temporal axes represent extraction periods. Yellow marks in the same axes represent the dates of the plotted images.

Figure 5. Well field (zone 1) and Pozuelo de Alarcón area (zone 3) average displacements. Zone 3 shows a continuous subsidence during first set and a lower amplitude movement during the second. Zone 1 fits better with the aquifer extractions and recoveries.

Figure 6. a) Differential displacement for every extraction - recovery phase. b) Differential displacement for every extraction-recovery phase with respect to the well field distance. Extraction–Recovery cycle duration is shown in table 1.

Figure 7. Total displacements divided into elastic and inelastic components of deformation (FE-1).

Figure 8. a) Surface movements and underground water position for well FE-1, Green line shows the model calibration area. b) Strain-stress curve for well FE-1. S_{ke} is the elastic storage coefficient.

Figure 9. Piezometric level, DInSAR and modeled displacements time series for six wells from the study area including FE-1. See wells location in figure 1.

Figure 1

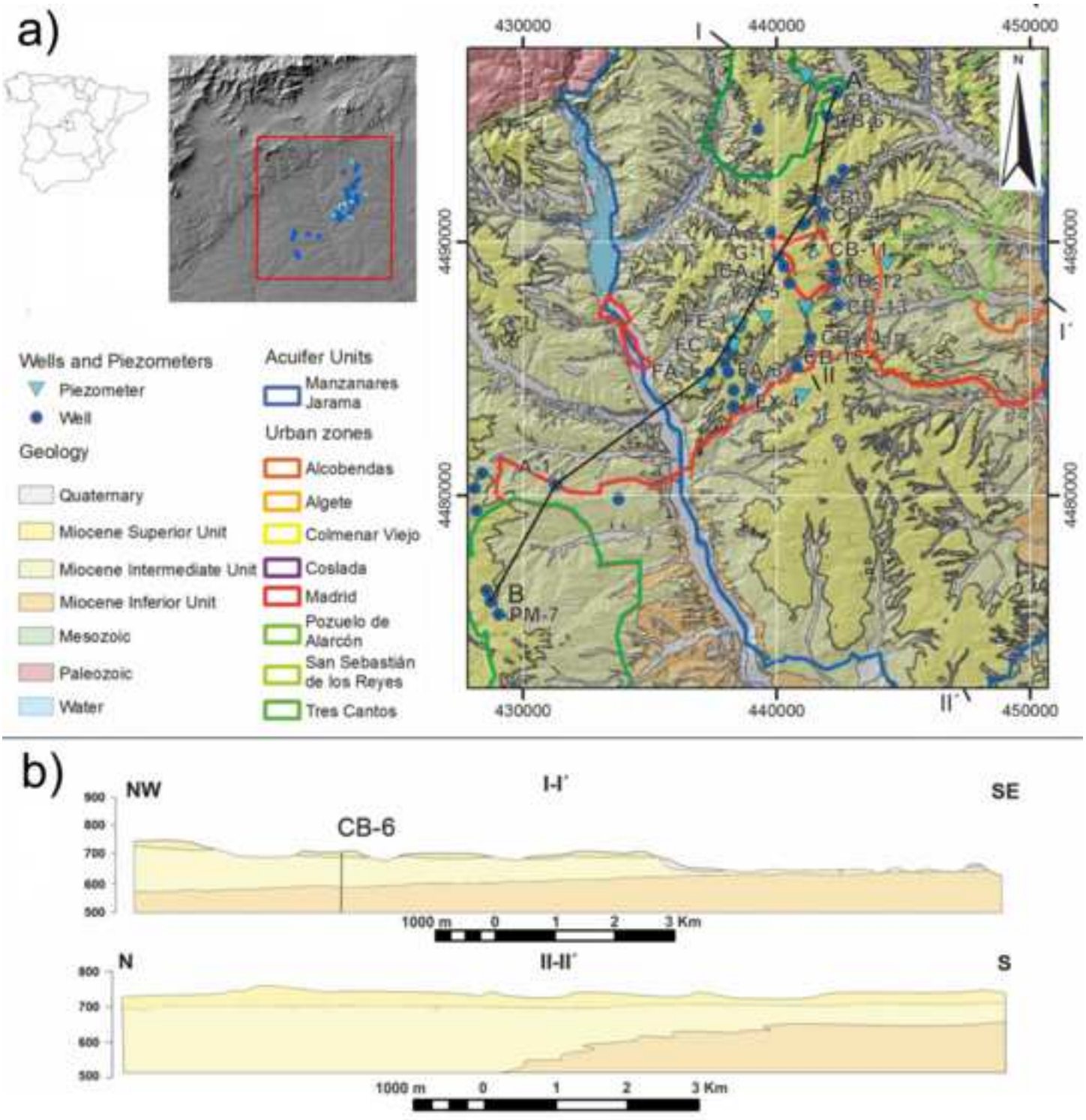

Figure 2

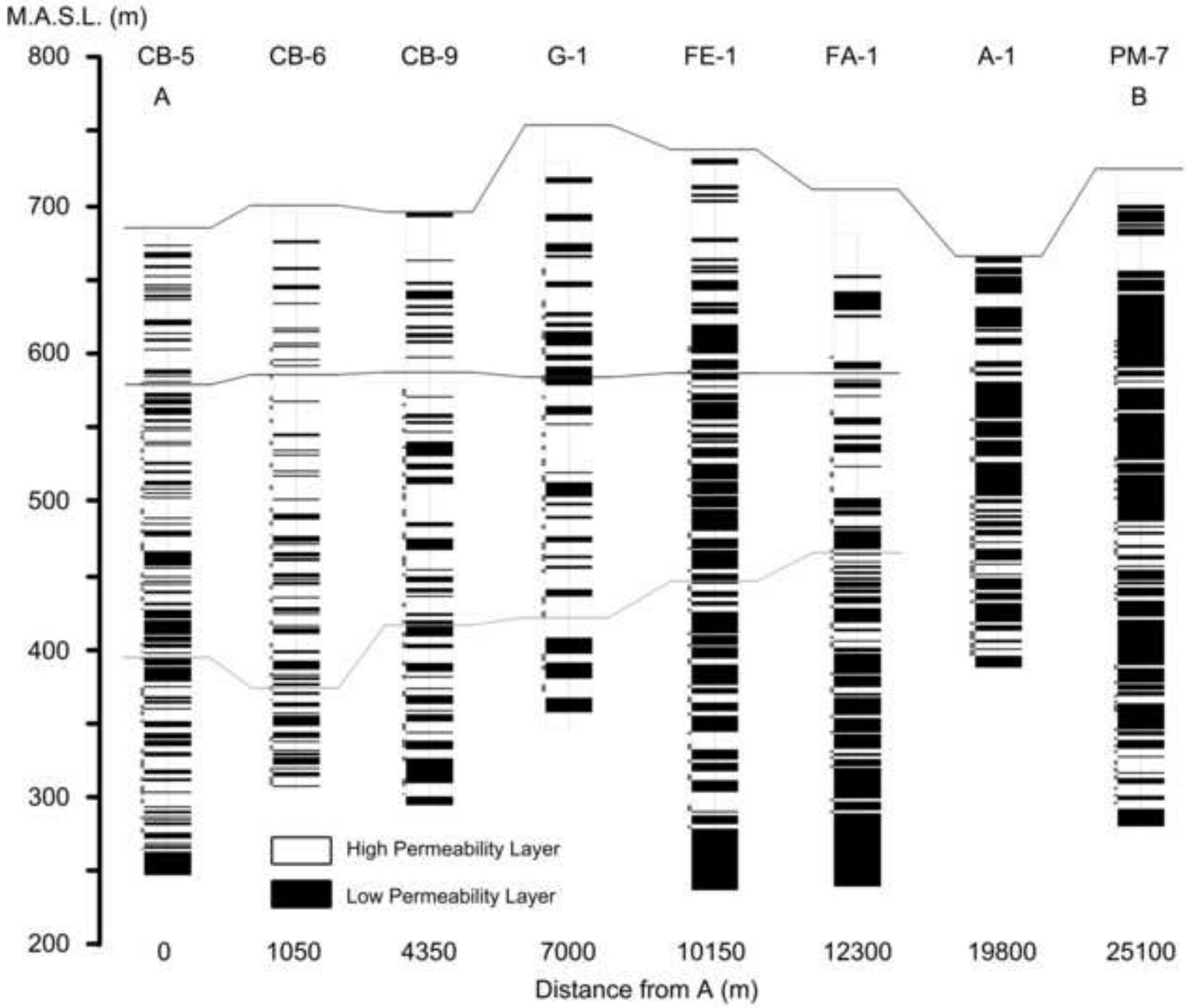

Figure 3

Figure 4

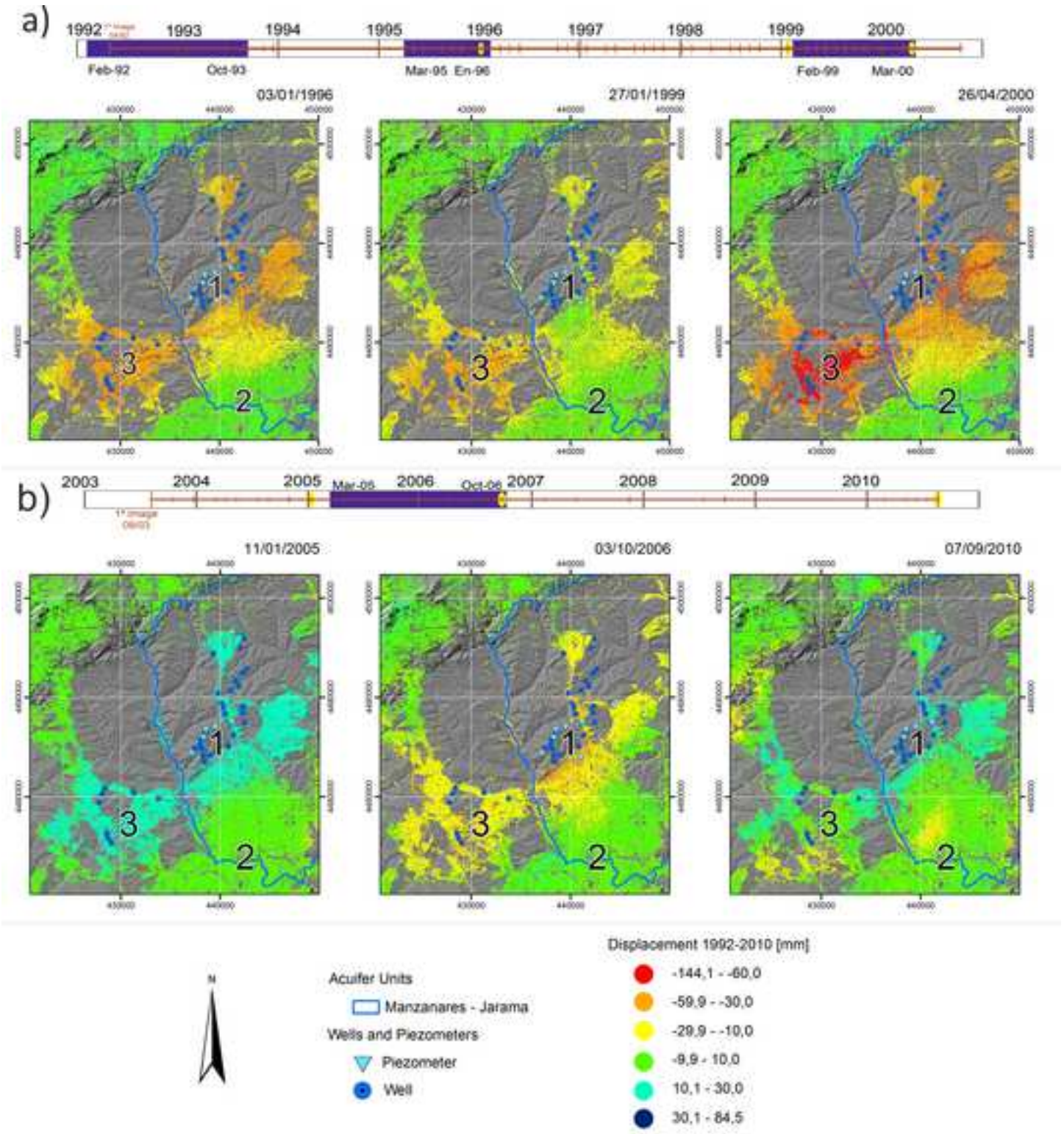

Figure 5

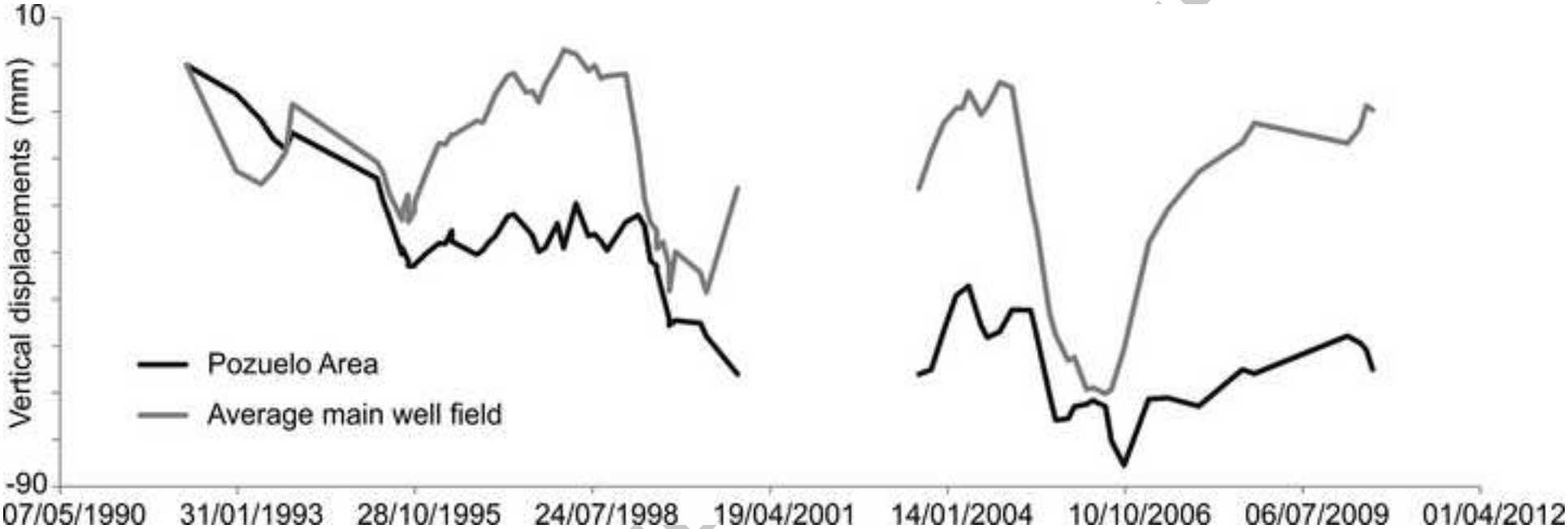

Figure 6

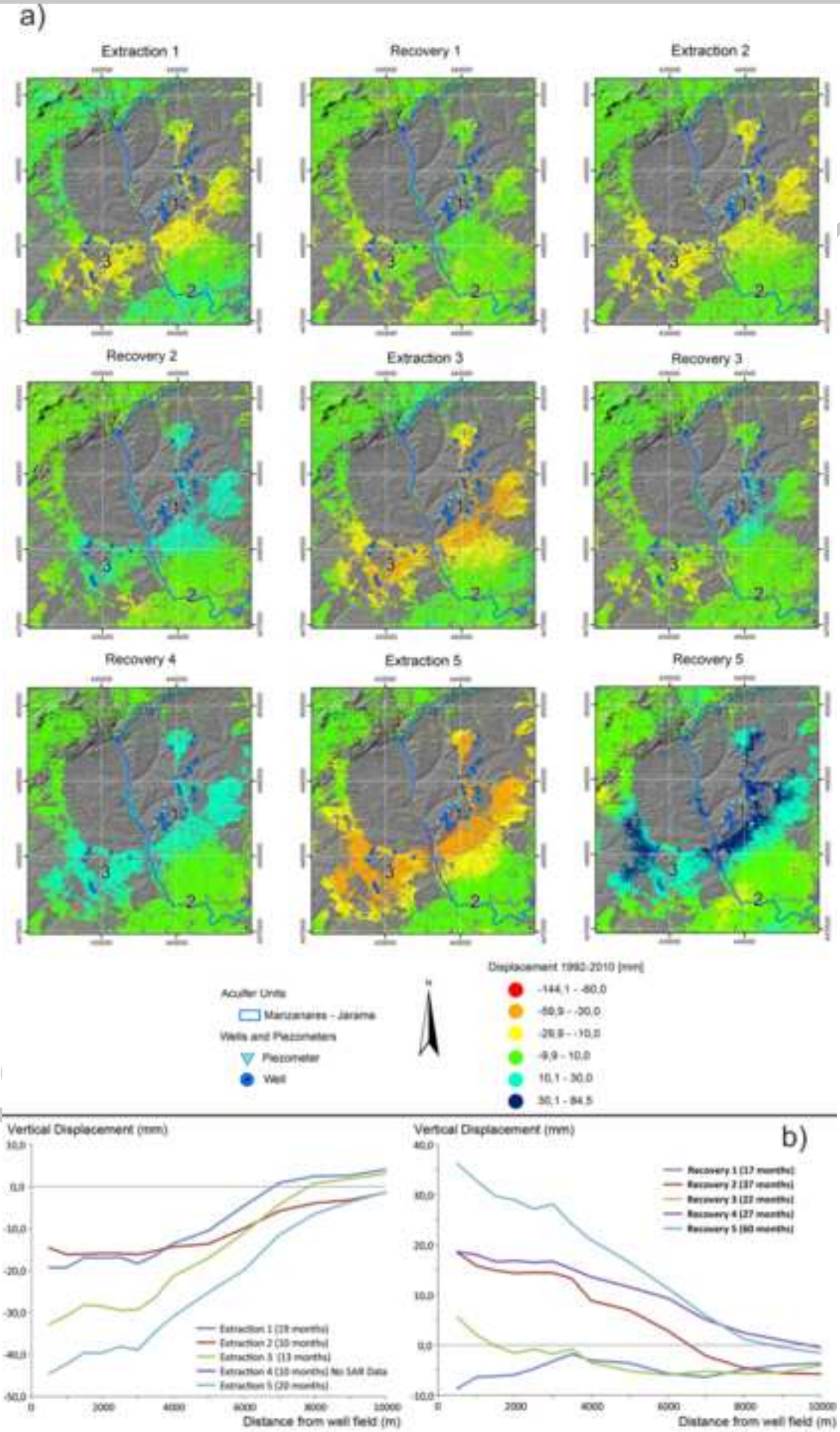

Figure 7

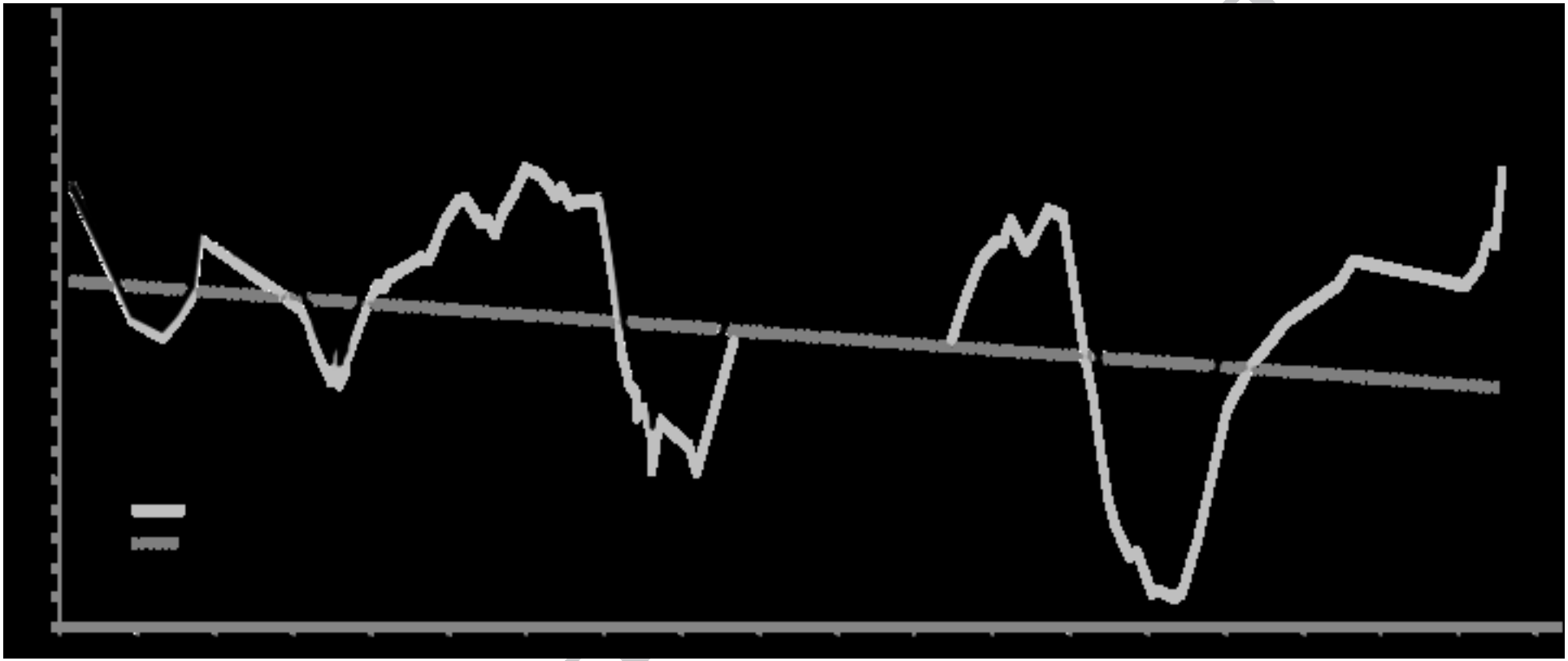

Figure 8

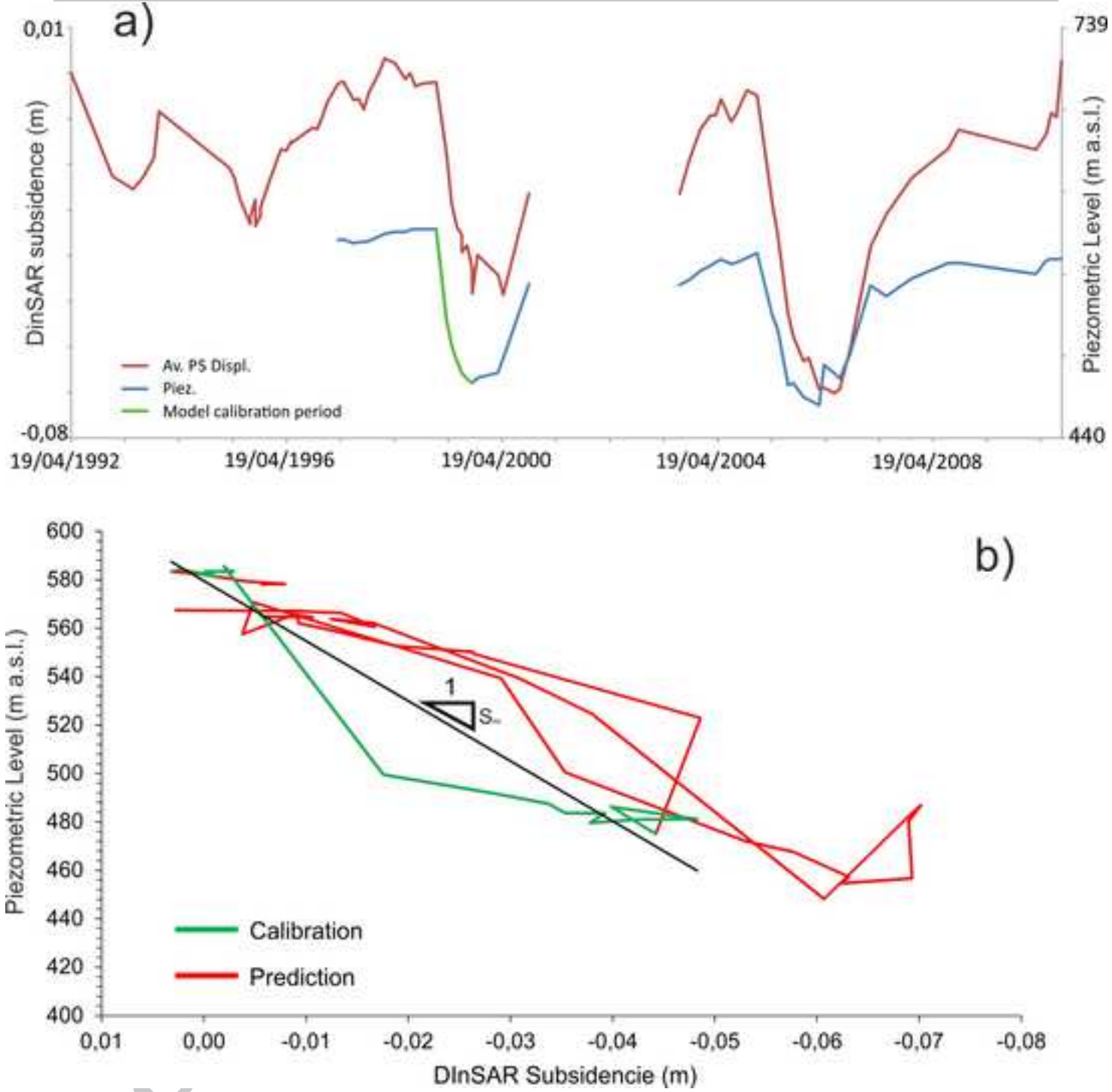

Figure 9

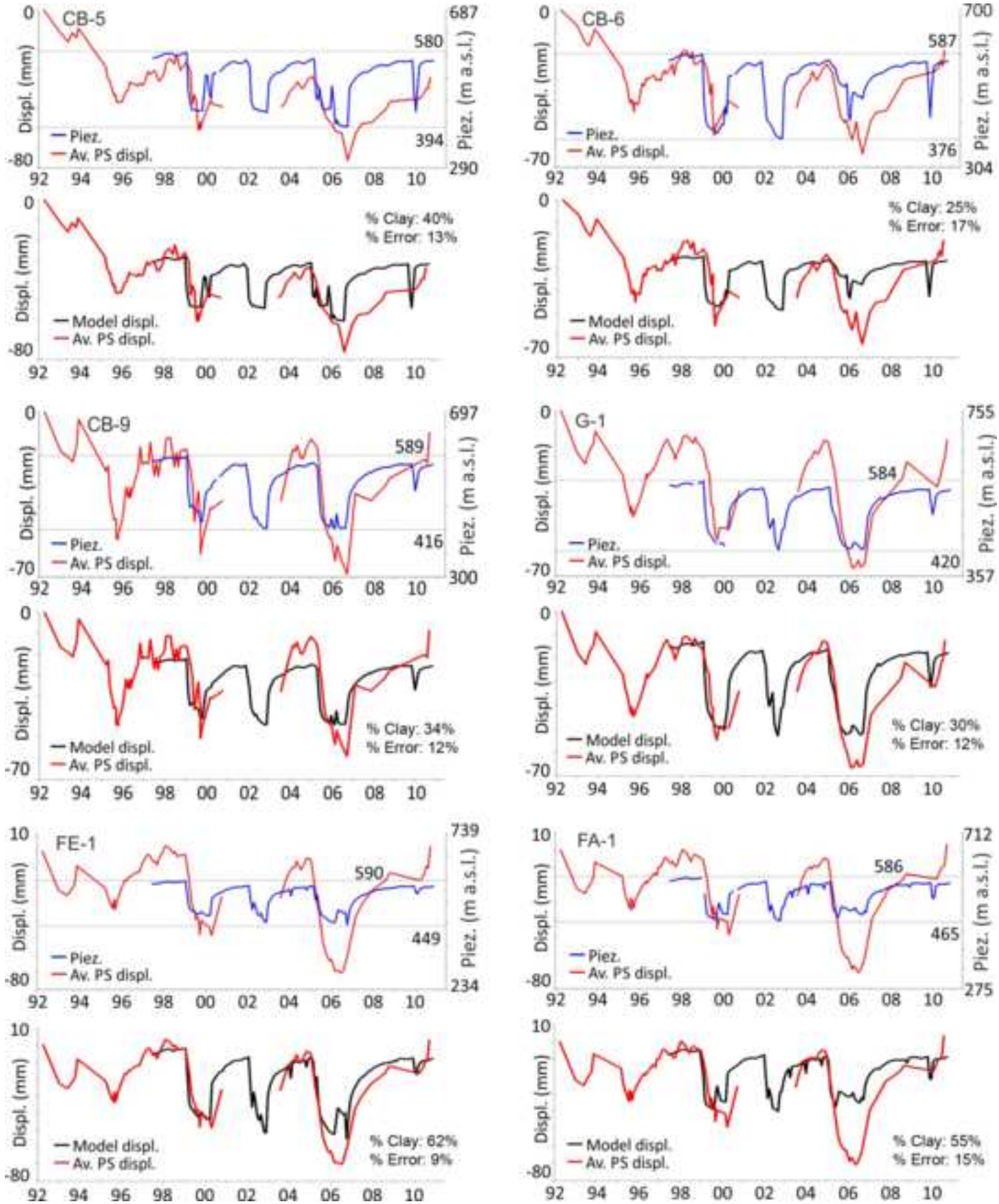

Table 1. Dates and duration of each extraction – recovery cycle

Cycle	Phase	Start date	End date	Duration (months)	Piezometric displacement		Average velocity (mm/year)	Average displacement (mm)
					Max (m)	Mean (m)		
Cycle 1	Extraction 1	Mar. 1992	Sep. 1993	19	n/a	n/a	-8,07	-10,2
	Recovery 1	Oct. 1993	Feb. 1995	17			-2,11	-2,8
Cycle 2	Extraction 2	Mar. 1995	Dec. 1995	10	n/a	n/a	-14,7	-11,2
	Recovery 2	Jan. 1996	Jan 1999	36			2,28	8,8
Cycle 3	Extraction 3	Feb. 1999	Mar. 2000	13	-197.2	-131.9	-15,07	-15,9
	Recovery 3	Apr. 2000	Feb. 2002	22			n/a	n/a
Cycle 4	Extraction 4	Mar. 2002	Dec. 2002	10	-197.2	-128.7	n/a	n/a
	Recovery 4	Jan. 2003	Mar. 2005	27			6,68	9,6
Cycle 5	Extraction 5	Apr 2005	Nov. 2006	20	-173.7	-136.3	-12,28	-17,7
	Recovery 5	Dec. 2006	Dec. 2011	60			3,07	10,9

Table 2. Average differential displacement (mm) around the well field for every cycle and phase at different distances. SR: uplift-subsidence ratio (%); TR: cycle temporal ratio (adimensional)

Cycle	Phase	Distance from the well field (m)		
		7000	4000	500
Cycle 1	Extraction (mm)	-13.0	-17.3	-21.8
	Recovery (mm)	-2.9	-1.8	-1.0
	SR (%)	0.0	0.0	0.0
	TR	0.9	0.9	0.9
Cycle 2	Extraction (mm)	-13.0	-15.0	-13.8
	Recovery (mm)	12.8	18.9	25.0
	SR (%)	98.5	126.0	181.2
	TR	3.7	3.7	3.7
Cycle 3	Extraction (mm)	-20.6	-26.8	-35.1
	Recovery (mm)	-1.8	1.6	10.1
	SR (%)	0.0	6.0	28.8
	TR	1.7	1.7	1.7
Cycle 4	Recovery (mm)	12.6	16.3	18.5
	TR	2.7	2.7	2.7
Cycle 5	Extraction (mm)	-22.7	-30.8	-45.1
	Recovery (mm)	15.1	23.1	40.5
	SR (%)	66.5	75.0	89.8
	TR	3.0	3.0	3.0

Table 3. Clay percentage, Elastic storage coefficient (S_{ke}), S_w, Storage Coefficient (S) and elastic deformation/inelastic deformation ratio ($R_{ed/id}$) and for every well. The location of the different wells is shown in figure 1.

Well ID	Clay Percentage %	S_{ke}	S_w (Porosity 1-20%)	S	$R_{ed/id}$
CA-3	n/a	$2,59\times 10^{-4}$	n/a	n/a	4,82
CA-4	n/a	$2,53\times 10^{-4}$	n/a	n/a	3,63
CA-5	n/a	$2,87\times 10^{-4}$	n/a	n/a	4,70
CB-4	n/a	$2,20\times 10^{-4}$	n/a	n/a	4,39
CB-5	40	$1,70\times 10^{-4}$	$8,46\times 10^{-6}$ - $1,69\times 10^{-4}$	$1,78\times 10^{-4}$ - $3,39\times 10^{-4}$	1,91
CB-6	25	$1,12\times 10^{-4}$	$8,97\times 10^{-6}$ - $1,79\times 10^{-4}$	$1,21\times 10^{-4}$ - $2,91\times 10^{-4}$	3,02
CB-9	34	$1,82\times 10^{-4}$	$8,46\times 10^{-6}$ - $1,69\times 10^{-4}$	$1,90\times 10^{-4}$ - $3,51\times 10^{-4}$	7,76
CB-11	51	$2,60\times 10^{-4}$	$5,43\times 10^{-6}$ - $1,09\times 10^{-4}$	$2,65\times 10^{-4}$ - $3,69\times 10^{-4}$	4,84
CB-12	n/a	$4,07\times 10^{-4}$	n/a	n/a	4,91
CB-13	n/a	$3,89\times 10^{-4}$	n/a	n/a	10,36
CB-14	n/a	$3,31\times 10^{-4}$	n/a	n/a	2,86
CB-15	n/a	$4,68\times 10^{-4}$	n/a	n/a	1,66
FA-1	55	$2,96\times 10^{-4}$	$5,66\times 10^{-6}$ - $1,13\times 10^{-4}$	$3,02\times 10^{-4}$ - $4,09\times 10^{-4}$	3,94
FA-3	n/a	$3,57\times 10^{-4}$	n/a	n/a	5,46
FC-2	n/a	$3,63\times 10^{-4}$	n/a	n/a	3,80
FX-4	n/a	$4,14\times 10^{-4}$	n/a	n/a	3,01
G-1	30	$2,44\times 10^{-4}$	$7,68\times 10^{-6}$ - $1,54\times 10^{-4}$	$2,52\times 10^{-4}$ - $3,98\times 10^{-4}$	3,37
FE-1	62	$3,77\times 10^{-4}$	$4,83\times 10^{-6}$ - $9,66\times 10^{-5}$	$3,82\times 10^{-4}$ - $4,74\times 10^{-4}$	3,61

Well field media	42	$2,99\times 10^{-4}$	$7,07\times 10^{-6}$ - $1,41\times 10^{-4}$	$2,41\times 10^{-4}$ - $3,76\times 10^{-4}$	4,34
Well field standard deviation	14	$9,30\times 10^{-5}$	$1,71\times 10^{-6}$ - $3,42\times 10^{-5}$	$8,67\times 10^{-5}$ - $5,81\times 10^{-5}$	2,05

Table 4. Average model error and percentage error for each period. See wells location in figure 1.

	Average difference between model and InSAR time series					
	Complete Period		Period 1 (1997-2000)		Period 2 (2003-2010)	
	Average error (mm)	Percentage error %	Average error (mm)	Percentage error %	Average error (mm)	Percentage error %
CA-3	6,7	14	6,0	15	7,3	13
CA-4	7,0	12	4,9	12	8,6	16
CA-5	5,7	10	4,7	11	6,5	12
CB-4	7,7	12	5,9	12	9,1	15
CB-5	7,1	13	5,4	14	8,3	19
CB-6	7,6	17	6,1	16	8,8	19
CB-9	7,4	12	6,4	13	8,1	13
CB-11	6,1	13	5,6	14	6,6	14
CB-12	6,5	12	5,7	12	7,2	15
CB-13	6,5	12	6,2	11	6,8	14
CB-14	7,6	13	6,2	13	8,6	17
CB-15	12,2	17	9,0	17	14,7	26
FA-1	10,8	15	7,7	16	13,2	18
FA-3	8,9	11	8,0	16	9,4	12
FC-2	17,4	24	14,1	27	19,9	27
FX-4	9,4	12	9,0	15	9,8	14
G-1	6,5	12	5,1	12	7,5	14
FE-1	6,8	9	4,5	9	8,5	12
Well field mean	8,2	13	6,7	14	9,4	16
Well field standard deviation	2,8	3	2,3	4	3,4	4

- We study surface subsidence in a well field area related with underground water level.
- We monitor surface subsidence with DInSAR methods.
- Water extraction and recovery related with subsidence and uplift detected.
- An elastic model for surface behavior has been performed.
- A quasi-perfect elastic terrain behavior is presented.